ICAS 2016
30th Congress of the International Council of the Aeronautical Sciences
DCC, Daejeon, Korea ; September 25-30, 2016

FLOW CONTROL ON HELICOPTER-ROTOR BLADES VIA ACTIVE GURNEY FLAP

Wienczyslaw Stalewski*
***Institute of Aviation, Poland**

Keywords: *helicopter rotor blades, flow control, Active Gurney Flap, rotorcraft performance*

Abstract

The Active Gurney Flap (AGF) is a small, flat tab cyclically deployed and retracted at lower surface of the rotor blade near its trailing edge. It is expected that the device may improve performance of modern helicopters. The main goal of presented investigations was to develop research methodology and next to use it in studies on phenomena occurring in the flow around helicopter-rotor blades equipped with AGF. Conducted CFD simulations aimed at validation of the developed methodology as well as at significant supplementing and extension of results of experimental research. Simplified sensitivity analysis has been conducted aiming at determination of geometric and motion-control parameters of the AGF, optimal from point of view of helicopter-performance improvement.

1 Introduction

Active flow control on helicopter-rotor blades is one of promising directions of development in Rotorcraft Engineering, aiming at improvement both the performance and environmental impact of modern helicopters.

Flow on rotor blades may be controlled by different means, including: fluidic devices [1], vortex generators [2] or mechanical devices mounted in proximity of blade trailing edge [3]. The solution presented in this paper belongs to the third of above groups and is named Active Gurney Flap (AGF).

The classic Gurney Flap [4] is a small, flat tab located at a pressure side of lifting surface near its trailing edge. The tab deflects the air stream behind the trailing edge downwards, leading to lift increase. In helicopter applications, instead of static tab, the dynamically deployed and retracted Gurney flap is more useful, because of strong dynamic effects in flow during rotorcraft flight.

In Rotorcraft Engineering, the Active Gurney Flap is a small, flat tab located at lower surface of the blade near its trailing edge. The tab is cyclically deployed and retracted perpendicularly to the blade surface. When deployed, the tab deflects air stream behind the trailing edge downwards, leading to lift increase, which is especially important on the retreating blade of the rotor. On the advancing blade, the AGF is retracted to minimise rotor torque. Such performance-enhancement application of the AGF is realised in one deployment-retreatment cycle per one revolution of the rotor. Higher frequencies of AGF motion are considered for vibration-control purposes. Due to technical limitations, the deployable tab is usually located at certain distance from the trailing edge of the blade, as shown in Fig. 1.

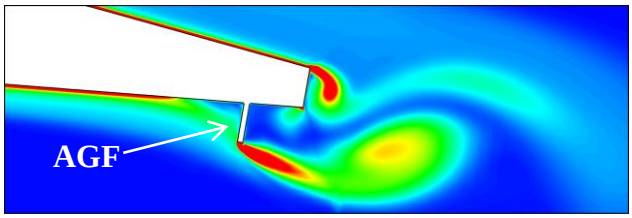

Fig. 1 Vortex structures around a trailing edge of the blade with fully deployed Active Gurney Flap.

The AGF-type device, through active control of the flow on the blades may significantly improve aerodynamic properties of the rotor. However, to take full advantage of potential benefits of AGF applications it is necessary to gain knowledge about physical phenomena that

occur in the flow around such configurations. Eventually, the knowledge should help to answer the question: how to design, implement and control the AGF-type devices so as to gain maximum profits, e.g. significant improvement of helicopter performance.

Investigations presented in the paper have focused on the topics formulated above and have been conducted based on computational-research methodology within the EU 7th FWP Project COMROTAG ("Development and Testing of Computational Methods to Simulate Helicopter Rotors with Active Gurney Flap") realised for the Clean Sky Joint Technology Initiative.

2 Methodology

The general scheme of developed methodology of simulation of forward flight of helicopter main rotor is shown in Fig. 2. In the presented approach, the simulation of rotor flight consists in the solution of unsteady Navier-Stokes Equations in time-varying domain surrounding the rotating rotor. The Navier-Stokes Equations are solved using the commercial code ANSYS FLUENT [6]. All computational activities concerning specific rotorcraft aspects, including the AGF motion, are performed by the developed code Virtual-Rotor-3D which is compiled module of User Defined Functions, linked with essential code of ANSYS FLUENT. Among others, the module Virtual-Rotor-3D is responsible for modelling of:

- rotor forward flight and rotational motion
- feathering of the rotor blade, resulting from assumed collective and cyclic pitch controls and pitch-flap coupling
- flap and lag motion of the blades around flap and lag hinges
- cyclic motion of the AGF

Coupled equations of flap and lag motion of the blades are solved simultaneously with the solution of Navier-Stokes Equations, taking into account effects of dampers and springs, if any. The flap-and-lag motion is described by the system of four ordinary differential equations of the first order on four unknown functions: $\beta(t)$, $\zeta(t)$, $\beta(\dot{t})$, $\zeta(\dot{t})$, where β is the flap angle, ζ is the lag angle, $\dot{\beta}=d\beta/dt$, $\dot{\zeta}=d\zeta/dt$.

The blade pitch controls may be changed during the simulation which is used when trimming the rotor so as to obtain required thrust and moments. Alternative trimming procedure, so called "zero-flapping" consists in establishing the cyclic pitch controls so as to obtain zero 1st-harmonics of blade flapping.

The input data consist of computational mesh and three data sets describing: flight conditions, flight controls and rotor data.

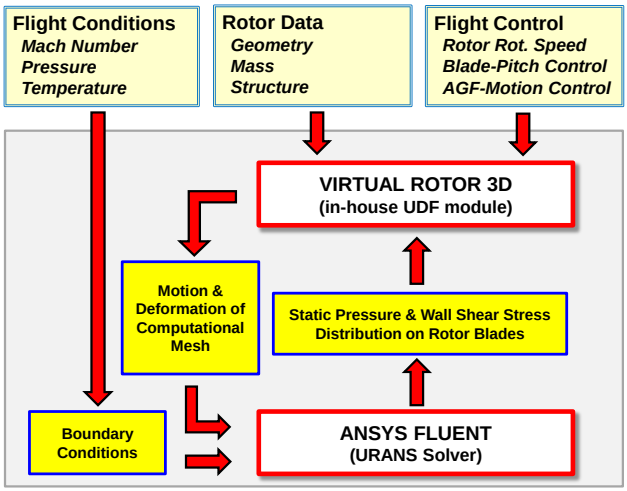

Fig. 2 The general scheme of developed methodology of simulation of flight of helicopter main rotor with blades equipped with AGF.

In the presented approach, the computational mesh is divided into several sub-domains. Around each blade, the cylinder-conical volume zone is defined, as it is shown in Fig. 3. Such zones are embedded in a cylinder-volume zone which is embedded in a far-field, cuboid zone. The overall topological structure of the mesh is presented in Fig. 4. During the rotor flight simulation, the mesh surrounding each blade is moving together with the blade. This motion is a combination of feathering, flapping and lead-lag motion. Additionally the mesh surrounding each blade is rotating together with the cylindrical zone, around the rotor-rotation axis. The motion of meshes surrounding the blades, relative to the cylindrical zone, is realised by the use of Dynamic Mesh and Sliding Mesh techniques implemented in the ANSYS FLUENT solver. The rotational motion of the cylindrical zone inside the far-field zone is also realised based on the Sliding Mesh technique.

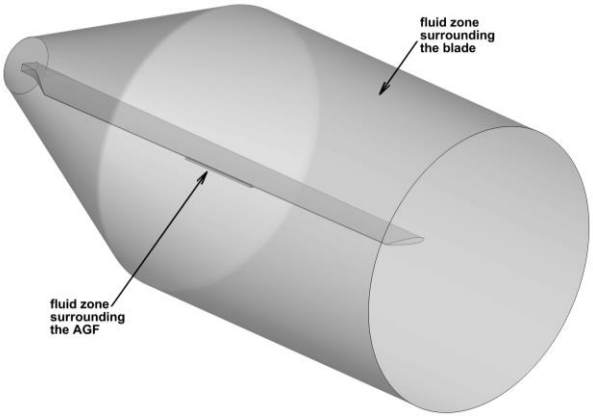

Fig. 3. The cylinder-conical zone surrounding each of the rotor blades.

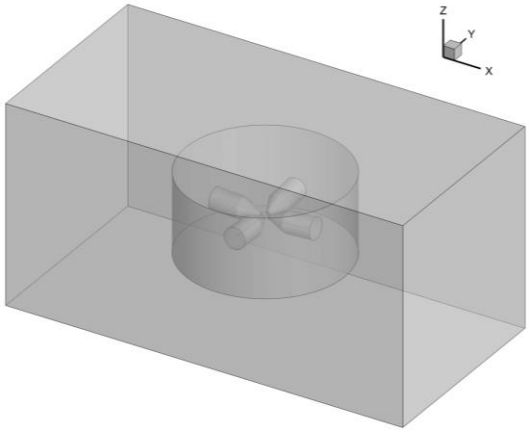

Fig. 4. Overall topology of computational mesh.

The mesh inside a separate volume zone surrounding the AGF is locally deformed so as to model the AGF motion, as shown in Fig. 5. The developed method of the AGF motion ensures high quality of deformed mesh as well as full repeatability of deformations. The method is an alternative to the Overlapping Grid Methods [5], usually used to model the flow around the AGF.

3 Computational Studies on Flow Control on Rotor Blades via Active Gurney Flap

Computational studies conducted in the program COMROTAG have been aiming at:

- validation of developed and implemented CFD codes against results of WTT,
- significant gain of knowledge about flow control through Active Gurney Flap in rotorcraft applications,
- conduction of computer simulations prior to flight tests of real rotor/helicopter (so called "blind tests"), in order to define the optimal scope of flight tests as well as to identify potentially dangerous phases of flight.

Computational studies have been conducted for both the 2D and 3D configurations.

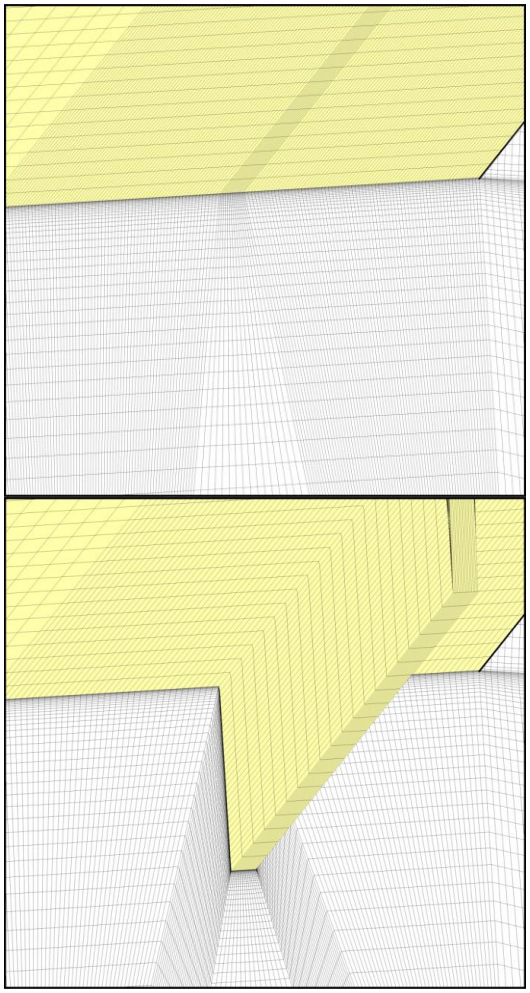

Fig. 5. 3D-mesh in proximity of fully retracted AGF (upper graph) and fully deployed AGF (lower graph).

3.1 Two-Dimensional Studies on Flow Control via AGF

3.1.1 Computational Simulations of 2D WTT of Blade Segment Equipped with AGF

The subject of conducted two-dimensional experimental studies on AGF was the blade segment NACA0012 with thickened trailing edge and equipped with AGF. The angle of attack of the segment was fixed during every run, while the AGF was cyclically deployed and retracted. The same conditions were modelled in CFD simulations, including modelling of the three-dimensional space of the test-chamber inside. For these quasi-2D simulations,

simplified version of the developed software (Virtual-Rotor-2.5D) intended to solve such problems has been used. Presented results refer to WTT conducted for flow velocity V=60m/s, 5Hz frequency of AGF oscillations and ramp schedule of AGF motion shown in Fig. 6.

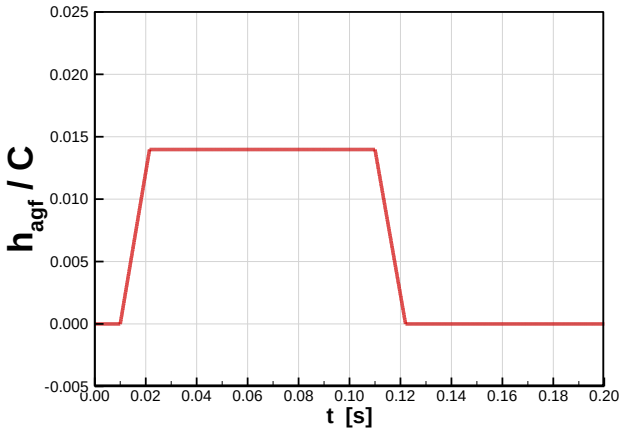

Fig. 6. Momentary height of the AGF (h_{agf}) vs. time (t) during one period of AGF deployment-retraction cycle.

For the case of angle of attack α=4deg, Fig. 7 compares the CFD and WTT results in respect to time-variable lift coefficient C_L measured during one period of AGF deployment-retraction cycle. While the time averaged computational and experimental values of C_L are similar, the computational result indicates strong oscillations, especially in the phase when the AGF is fully deployed. Such phenomenon is not observed in experimental results.

Presented in Fig. 8 frequency-domain analysis of time-varying pitching-moment coefficient (C_m) shows, that for CFD results the dominant frequency of oscillations of global aerodynamic coefficients is approximately 545 Hz, which is close to 566 Hz - the dominant frequency of unsteady vortex shedding observed in other CFD results related to the static case with fully deployed AGF and α=0deg. Fig. 8 shows also dominant, but much weaker frequency 1100 Hz, which is close to 1123 Hz - the dominant frequency of unsteady vortex shedding observed in another CFD results concerning the static case with retracted AGF and α=0deg. Unfortunately, the frequency-domain analysis of the experimental results does not indicate any dominant frequencies neither in proximity 592 Hz nor in proximity 1075 Hz, despite that these dominant frequencies were observed previously in WTT results in the static cases for both the AGF fully deployed and fully retracted (α=0deg).

This is all the more surprising since the PIV results confirm the occurrence of unsteady vortex shedding in the discussed experimental case. One of possible explanation of this incoherence of WTT results is that the pressure-measuring signals were filtered, so the higher frequencies have been cut.

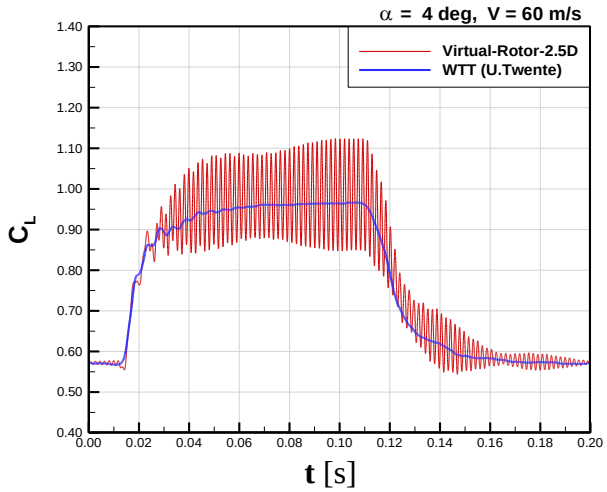

Fig. 7. Momentary lift coefficient (C_L) vs. time (t). Comparison of CFD and WTT results. Test case: α=4deg, V=60m/s.

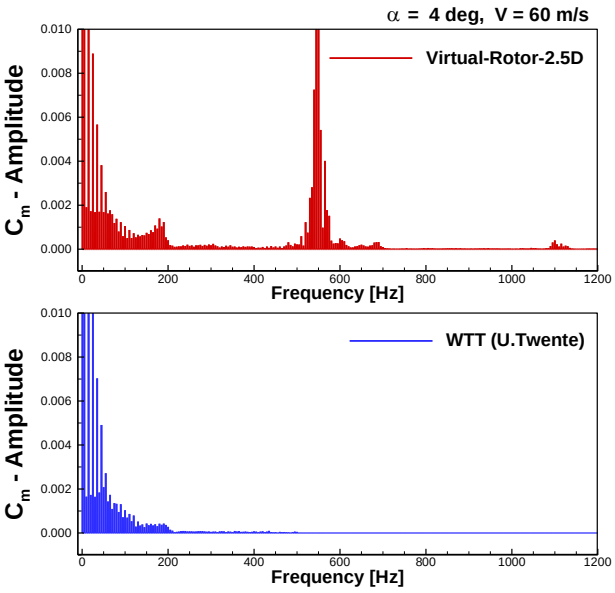

Fig. 8. Frequency-domain analysis of pitching moment coefficient C_m. Comparison of CFD and WTT results. Test case: α=4deg, V=60m/s.

Exemplary comparison of PIV results obtained in WTT and results of CFD concerning Q-criterion contours is presented in Fig. 9.

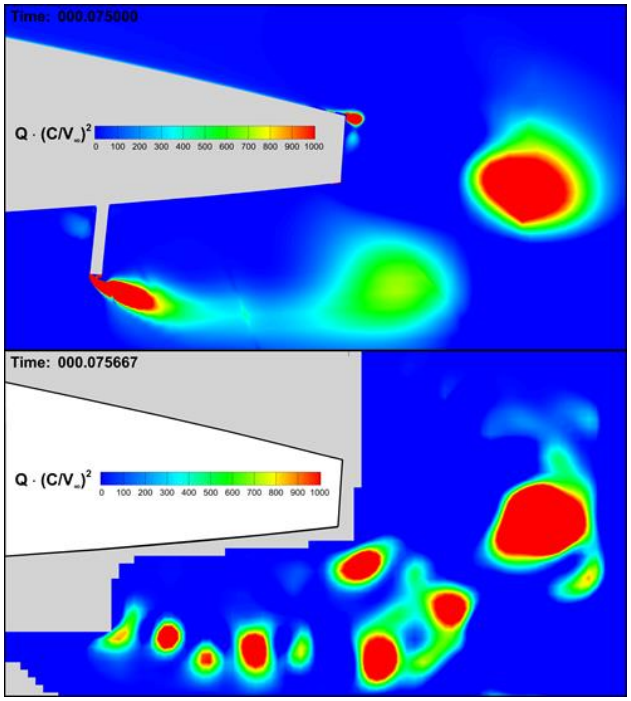

Fig. 9. Q-criterion contours at a moment of fully deployed AGF. Comparison of results of CFD (top) and WTT (bottom). Test case: α=4deg, V=60m/s.

The second simulation has been conducted for α=12deg, V=60m/s. Fig. 10 compares CFD and WTT time-variable lift coefficient C_L measured during one period of AGF deployment-retraction cycle. The values of computational and experimental coefficient C_L are similar, also in terms of amplitudes and frequencies of oscillations of global coefficients. In this case there are no high dominating frequencies of unsteady vortex shedding. It is likely, that it is a results of trailing-edge separation, which makes the vorticity flowing from the upper surface of the blade much weaker than in fully attached flow. This leads to weakening of the effect of counter rotating vortices flowing from upper and lower part of the trailing edge. Thus, the effect of unsteady vortex shedding is significantly reduced in this case.

Computational and experimental results related to the pressure coefficient (C_P) distribution for the case: α=12deg, V=60m/s are compared with each other for time moments corresponding to the AGF fully retracted in Fig. 11 and fully deployed in Fig. 12. These results confirm the hypothesis of flow separation on the upper surface of the airfoil, because they indicate characterising separated flows under-pressure at the trailing edge.

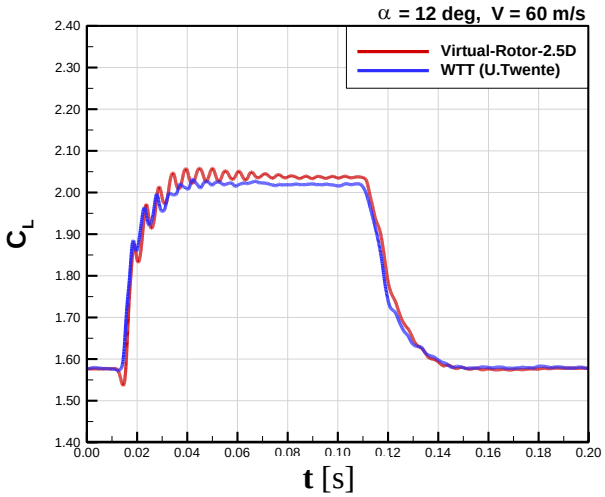

Fig. 10. Momentary lift coefficient (C_L) vs. time (t). Comparison of CFD and WTT results. Test case: α=12deg, V=60m/s.

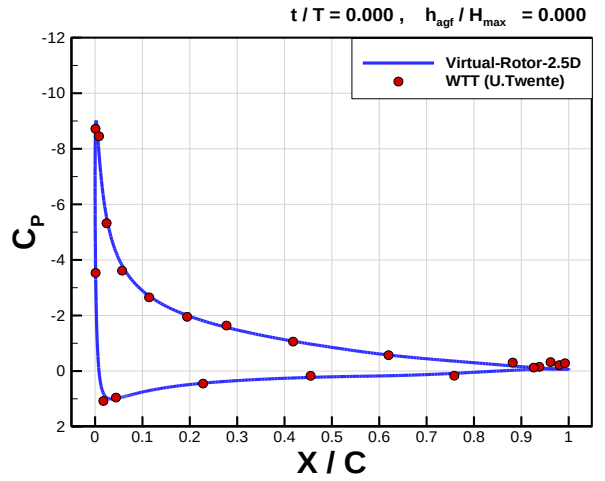

Fig. 11. Comparison of CFD and WTT results related to pressure-coefficient (C_P) distribution for AGF fully retracted. Test case: α=12deg, V=60m/s.

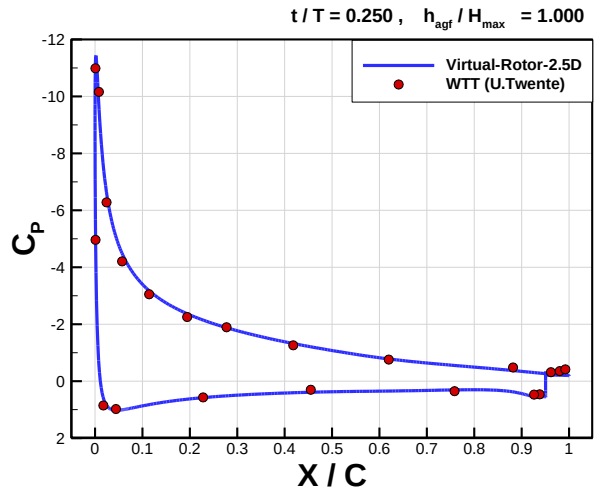

Fig. 12. Comparison of CFD and WTT results related to pressure-coefficient (C_P) distribution for AGF fully deployed. Test case: α=12deg, V=60m/s.

3.1.2 Sensitivity Analysis

Based on 2D version of the developed software a sensitivity analysis has been conducted. The investigations were focused on searching for chordwise position and maximum height of the AGF, optimal from point of view of increase of lift force generated by a retreating blade.

The subject of conducted simulations was airfoil NACA0012 with thickened trailing edge. As it is shown in Fig. 13, angle of attack (α) of the airfoil was changed harmonically with frequency 5Hz, within the range: 1deg ÷ 10deg. Simultaneously the free-stream Mach number (M) was changing within the range: from 0.15 for maximum angle of attack (retreating-blade-flow conditions) to 0.55 for minimum angle of attack (advancing-blade-flow conditions). The oscillating airfoil was equipped with the AGF deployed/retracted according to the sinusoidal schedule shown in Fig. 13. In the conducted sensitivity analysis three chordwise positions of the AGF (X_{agf}) at 96%, 98% and 100% of airfoil chord (C) were considered and four maximum deployments of the AGF (H_{max}): 0.5%, 1%, 1.5% and 2% of airfoil chord. The investigations aimed at determination of correlations between parameters X_{agf}, H_{max} and the airfoil lift coefficient C_L (defined based on average dynamic pressure).

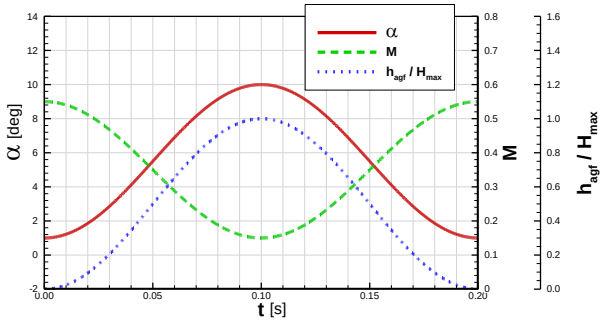

Fig. 13 Harmonic changes of angle of attack (a), free stream Mach number (M) and deployment of AGF (h_{agf}) assumed in conducted 2D sensitivity analysis.

Fig. 14 presents time-variable lift coefficient captured during one period of oscillations, for the clean airfoil and for twelve configurations of airfoil equipped with AGF. The oscillations of C_L visible in the presented graphs are the result of unsteady vortex shedding. Intensity and frequency of this phenomenon depends on parameters X_{agf}, H_{max} as well as on the phase of the airfoil motion. Generally it may be concluded that intensity and frequency of unsteady vortex shedding tends to decrease within retreating-blade phase (the highest angles of attack) which results from possible flow separations (which was discussed in previous sub-section), the highest deployment of AGF, which gives the effect of "the thickest trailing edge" of the airfoil and from the lowest flow velocities occurring on the retreating blade.

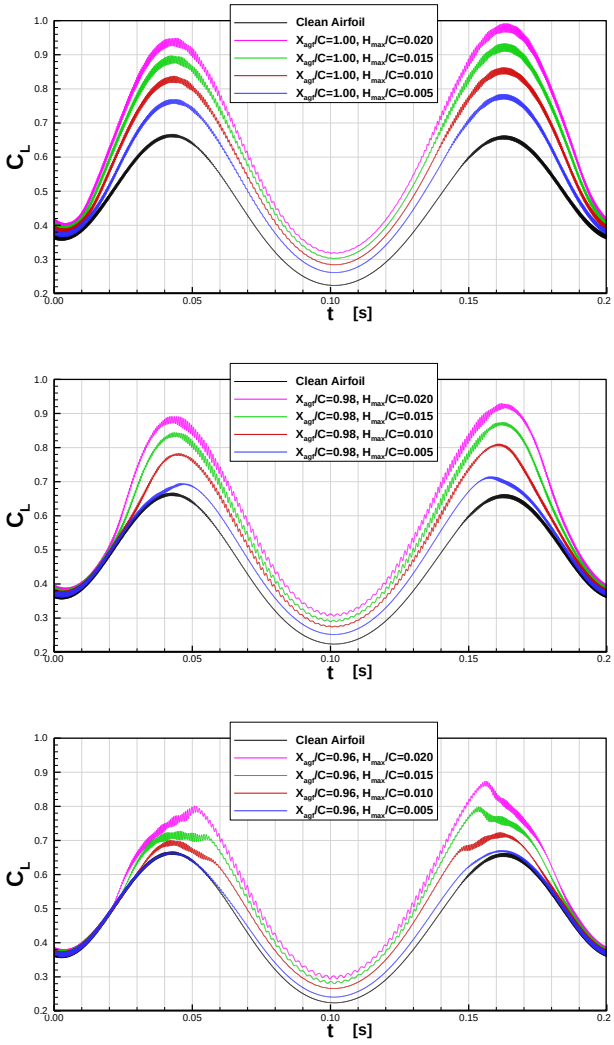

Fig. 14. Time-variable lift coefficient C_L captured during one period of oscillations, for the clean airfoil and for twelve configurations of airfoil equipped with AGF.

As opposed to the results discussed in the previous sub-section, where the ramp schedule of AGF deployment was applied, in the discussed simulations expressly dominant frequencies of unsteady vortex shedding have not been observed. This is the effect of continuous, harmonic changes of AGF height - one of the factors determining the unsteady

vortex-shedding frequency. As the result, in the presented simulations, for the cases with active AGF, whole spectrum of frequencies of unsteady vortex shedding was observed. Visualisations of vortex shedding for selected AGF configurations are presented in Fig. 15.

Fig. 16 presents lift-growth coefficient $\Delta C_{L(t)}$ as a function of AGF maximum height for three chordwise positions of the AGF. The coefficient $\Delta C_{L(t)}$ expresses difference of momentary lift coefficients $C_{L(t)}$ (defined based on momentary dynamic pressure) measured for the retreating-blade moment (t=0.10s), for given AGF configuration and for the clean airfoil.

Usually, the closer the AGF is placed to trailing edge, the smaller may be its maximum height. Therefore, the graph presented in Fig. 16, should help to find optimal compromise between position and height of designed AGF.

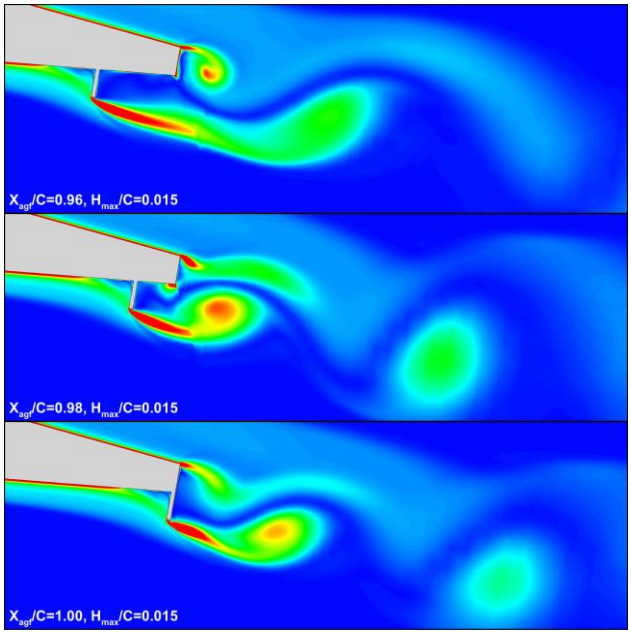

Fig. 15.Unsteady vortex shedding visualised through vorticity-magnitude contours, for maximum AGF deployment $H_{max}/C=0.015$ and for three chordwise positions of the AGF.

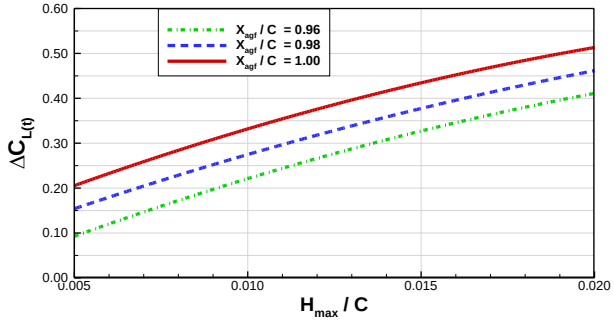

Fig. 16. Lift-growth coefficient ($\Delta C_{L(t)}$) measured on retreating-blade, as a function of the AGF max. height, for three chordwise positions of AGF.

3.2 Three-Dimensional Studies on Flow Control on Rotor Blades via AGF

Three-dimensional, computational studies on flow control on rotor blades via AGF, have been conducted for the case of the 4-blade, fully articulated model rotor of radius 1.1m. Rotor rectangular blades of chord 0.09m were equipped with AGF in spanwise position from 53.5% to 68.5% of rotor radius. The maximum deployment of AGF was 2.78% of blade chord. The preliminary computational tests were conducted for two reference configurations: 1) rotor with Clean-Blades, 2) rotor with blades equipped with fixed, Passive Gurney Flap (PGF). The essential tests have been conducted for three configurations of AGF, differing in presented in Fig. 17 schedules of AGF motion:

1) sinusoidal ($h_{agf} = H_{max}$: $\Psi = 270$deg),
2) ramp-1 ($h_{agf} = H_{max}$: $198\text{deg} \le \Psi \le 342\text{deg}$)
3) ramp-2 ($h_{agf} = H_{max}$: $243\text{deg} \le \Psi \le 297\text{deg}$)

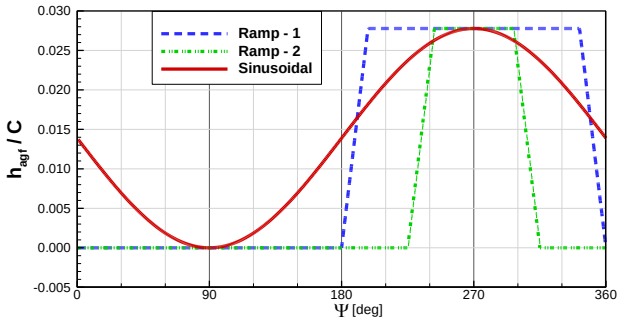

Fig. 17. Considered variants of AGF-motion schedules.

Rotor forward-flight tests were conducted for flight conditions: velocity 48m/s, rotor rotational speed 1600 rpm, zero pitch and bank angles of the rotor shaft, atmosphere: Sea Level ISA. For each configuration the forward-flight simulations have been conducted for several commanded angles of collective pitch: θ_0 = 4, 6, 8, 10 and 12 deg. In each single simulation, the components of commanded cyclic pitch: $\bar{\theta} = (\theta_S, \theta_C)$ were established so as to fulfil the "zero-flapping-trimming" requirements:

$$\bar{\beta}_1 = (\beta_{1S}, \beta_{1C}) = (0, 0) \qquad (1)$$

where β_{1S}, β_{1C} are 1st-harmonic components of blade flapping. According to applied iterative trimming procedure, corrected cyclic pitch $\bar{\theta}_n$ was evaluated according to the formula:

$$\bar{\theta}_n = \bar{\theta}_p - \left[\frac{\partial \bar{\beta}_1}{\partial \bar{\theta}}\right]^{-1} \cdot \bar{\beta}_{1p} \qquad (2)$$

where $\bar{\theta}_p$ is the current cyclic pitch, $\bar{\beta}_{1p}$ is the current vector $\bar{\beta}_1$ and $\left[\frac{\partial \bar{\beta}_1}{\partial \bar{\theta}}\right]$ is a gradient matrix. Selected results of CFD simulations conducted for two reference configurations: Clean-Blades and PGF, have been compared with analogous results of WTT [7]. Fig. 18 compares CFD and WTT results concerning dependency of torque coefficient (C_{QUS}) vs. thrust coefficient (C_{TUS}) (referenced to rotor solidity σ) for the Clean-Blades configuration. In this case the computational end experimental results agree with each other quite well. Differences are visible for the highest values of thrust coefficient where it is likely that significant retreating-blade stall occurs. Similar agreement of CFD and WTT results is visible in Fig. 19, where computational and experimental dependencies: torque coefficient (C_{QUS}) vs. thrust coefficient (C_{TUS}) are compared for the Passive-Gurney-Flap configuration.

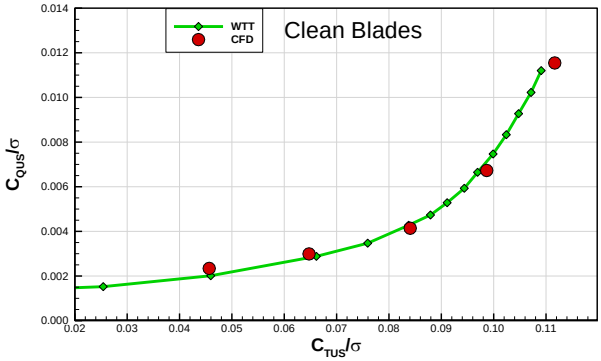

Fig. 18. Forward flight of Model Rotor at V=48m/s. Dependency (C_{QUS}/σ) vs. (C_{TUS}/σ). Results of CFD and WTT [7]. Clean-Blades configuration.

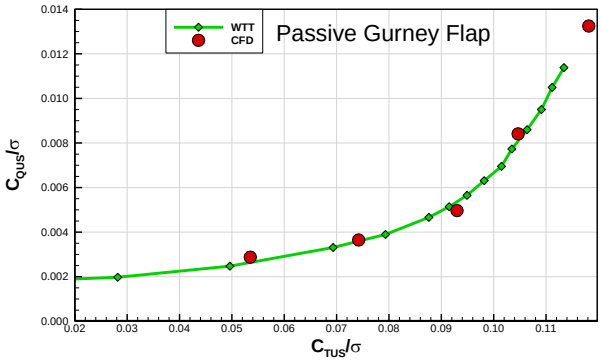

Fig. 19. Forward flight of Model Rotor at V=48m/s. Dependency (C_{QUS}/σ) vs. (C_{TUS}/σ). Results of CFD and WTT [7]. Passive-Gurney-Flap configuration.

Fig. 20 shows that application of PGF gives some performance benefits (i.e. generation of higher thrust for given torque) in comparison to Clean-Blades configuration but only above certain level of thrust coefficient (approx. C_{TUS}/σ >0.084). Analysing presented in Fig. 20 results for the configuration AGF(sinusoidal), it may be concluded, that for higher values of thrust, this configuration gives similar performance benefits as PGF configuration. For lower values of thrust the AGF(sinusoidal) configuration does not indicate power penalty, observed for the PGF configuration. The above conclusions concern also the AGF(ramp-1) configuration which is shown in Fig. 21. However, as it is shown in Fig. 22, the AGF(ramp-2) configuration does not indicate any significant performance benefits.

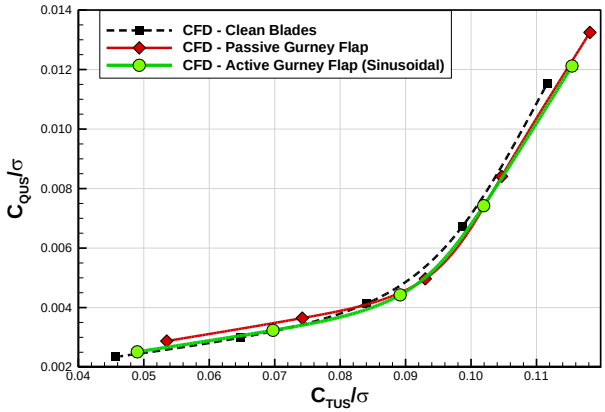

Fig. 20. Forward flight of Model Rotor at V=48m/s. Configurations: Clean-Blades, PGF and AGF(Sinusoidal). Dependency (C_{QUS}/σ) vs. (C_{TUS}/σ).

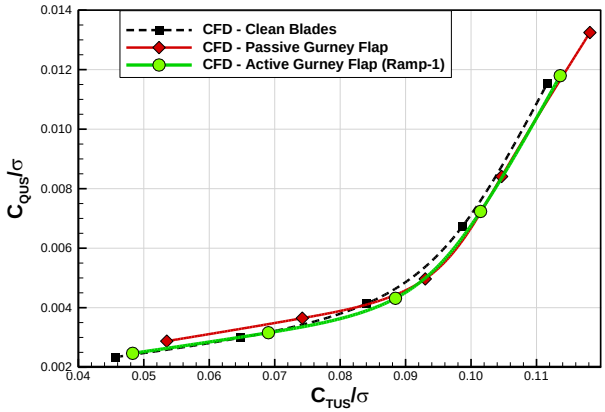

Fig. 21. Forward flight of Model Rotor at V=48m/s. Configurations: Clean-Blades, PGF and AGF(Ramp-1). Dependency (C_{QUS}/σ) vs. (C_{TUS}/σ).

Fig. 23 and Fig. 24 compare vortex structures (Q-criterion iso-surfaces) generated by Clean-Blades and AGF(sinusoidal) configurations, for two collective-pitch angles θ_0= 6 and 10 deg. As opposed to the case θ_0=6deg, for the case θ_0=10deg the strong retreating-blade stall is well visible for both compared configurations.

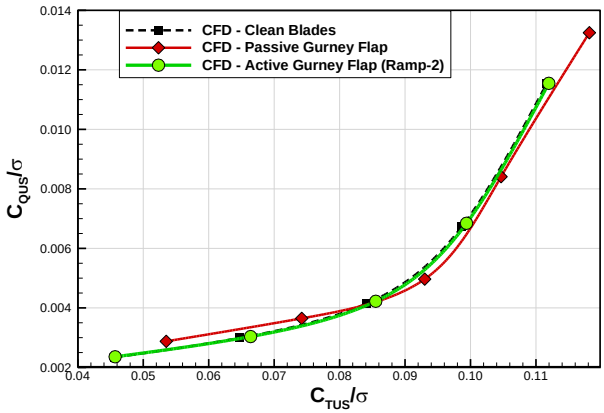

Fig. 22. Forward flight of Model Rotor at V=48m/s. Configurations: Clean-Blades, PGF and AGF(Ramp-2). Dependency (C_{QUS}/σ) vs. (C_{TUS}/σ).

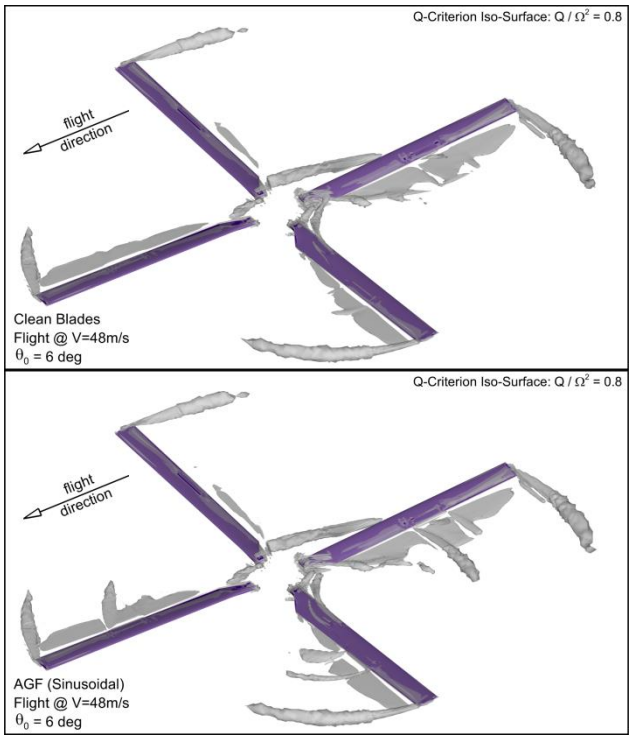

Fig. 23. Comparison of vortex structures for Clean-Blades and AGF(Sinusoidal) configurations. θ_0=6deg.

Moreover, the AGF configurations are characterised by significant vortex shedding at end-tips of deployed AGF, which is similar to formation of classic blade-tip vortices and which may be additional source of noise (however, this unfavourable phenomenon in case of Active Gurney Flap is significantly reduced compared to Passive-Gurney-Flap configuration). In the case of Clean-Blades configuration, at ends of the AGF zone the local thickening of the trailing edge may cause weak vortex shedding.

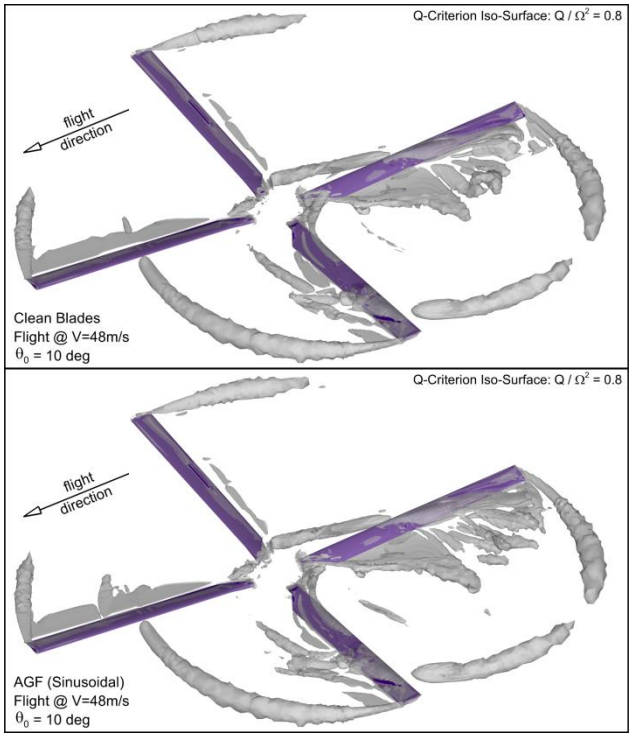

Fig. 24. Comparison of vortex structures for Clean-Blades and AGF(Sinusoidal) configurations. θ_0=10deg.

4 Conclusions

The investigations discussed in the paper focused on phenomena occurring in the flow around helicopter-rotor blades equipped with Active Gurney Flaps (AGF).

Validation of the developed CFD codes confirmed good agreement of computational and experimental results, concerning both the quasi-2D and 3D test cases.

Conducted simplified sensitivity analysis has aimed at determination of geometric and motion-control parameters of the AGF, optimal from point of view of helicopter-performance improvement.

Truly 3D studies on investigated phenomena have been conducted for the case of forward flight of model rotor, considering:

- two reference configurations: Clean-Blades and Passive Gurney Flap (PGF),
- three configurations with Active Gurney Flaps, differing in schedules of AGF motion: "sinusoidal", "ramp-1" and "ramp-2"

Performance benefits have been evaluated based on analysis of dependency: torque vs. thrust, favouring these configurations, which for given torque have generated the highest thrust.

Based on obtained computational results, it may be concluded that:

- For higher values of thrust (likely in presence of retreating-blade stall), the configurations with AGF give certain performance benefits in comparison to the Clean-Blades configuration, similar to the benefits of the PGF configuration.
- For lower values of thrust, the configurations with AGF, do not indicate the power penalty, observed for the PGF configuration.
- Above advantages of the AGF concern configurations of both the "sinusoidal" and "ramp-1" schedules of motion, but they do not concern the schedule "ramp-2" which has not indicated any performance benefits.
- Compared to the Clean-Blades configuration, the AGF configurations are characterised by significant vortex shedding at end-tips of deployed AGF.

Nomenclature

C	blade chord
C_L	lift coefficient
$C_{L(t)}$	lift coefficient based on moment. dyn. pressure
$\Delta C_{L(t)}$	coefficient of growth of $C_{L(t)}$
C_P	pressure coefficient
C_{QUS}	torque coefficient (US convention)
C_{TUS}	thrust coefficient (US convention)
h_{agf}	momentary height of AGF
H_{max}	maximum height of AGF
M	Mach number
Q	Q-criterion factor
t	time
V	velocity
X_{agf}	chordwise position of the AGF
α	angle of attack
β_{1S}, β_{1C}	1^{st}-harmonic components of blade flapping
θ_0	commanded collective pitch
θ_S , θ_C	components of commanded cyclic pitch
σ	rotor solidity
Ψ	blade azimuthal position
AGF	Active Gurney Flap
CFD	Computational Fluid Dynamic
PGF	Passive Gurney Flap
PIV	Particle Image Velocimetry
WTT	Wind Tunnel Tests

Acknowledgements

The research leading to these results was financed by the European Union's Seventh Framework Programme (FP7/2007-2013) for the Clean Sky Joint Technology Initiative under grant agreement No.CSJ-GA-2013-619627 and by the Ministry of Science of Poland from funds directed to supporting scientific research, under agreement No.3129/CLEANSKY/2014/2.

Computational support was obtained from University of Warsaw Interdisciplinary Centre for Mathematical and Computational Modelling, in the Computational Grant No.G52-4.

References

[1] Gardner A.D., Richter K., Rosemann H., Numerical Investigation of Air Jets for Dynamic Stall Control on the OA209 Airfoil, Proceedings of ERF 2010, Paris, 7-9 September 2010.

[2] Heine, B., Mulleners, K., Gardner, A., Mai, H., On the effects of leading edge vortex generators on an OA209 airfoil, ODAS2009, 2009.

[3] Feszty D., Gillies E.A., Vezza M., "Alleviation of Airfoil Dynamic Stall Moments via Trailing-Edge Flap Flow Control", AIAA Journal, Vol. 42, No. 1 (2004), pp. 17-25.

[4] Wang, J.J., Li Y.C., Choi K-S., Gurney flap - Life enhancement, mechanisms and applications, Progress in Aerospace Sciences 44 (2008), pp.22-47.

[5] Kinzel M.P., Maughmer M.D., Duque E.P.N, Numerical Investigation on the Aerodynamics of Oscillating Airfoils with Deployable Gurney Flaps, AIAA Journal Vol.48, No.7, July 2010.

[6] ANSYS, Inc., ANSYS FLUENT User's Guide. Release 15.0, November 2013. Available from: http://www.ansys.com.

[7] Gibertini G., Zanotti A., New Technique Implementation in GVPM, Deliverable Report of CleanSky Project GUM, GUM/WP2/D2.3, July 2015.

Copyright Statement